Electric-Field-Driven Dual Vacancies Evolution in Ultrathin Nanosheets Realizing Reversible Semiconductor to Half-Metal Transition

Mengjie Lyu,[†] Youwen Liu,[†] Yuduo Zhi,[†] Chong Xiao,[*,†] Bingchuan Gu,[‡] Xuemin Hua,[†] Shaojuan Fan,[‡] Yue Lin,[†] Wei Bai,[†] Wei Tong,[§] Youming Zou,[§] Bicai Pan,[†] Bangjiao Ye,[‡] and Yi Xie[*,†]

[†]Hefei National Laboratory for Physical Sciences at the Microscale, Collaborative Innovation Center of Chemistry for Energy Materials and [‡]State Key Laboratory of Particle Detection and Electronics, University of Science & Technology of China, Hefei, Anhui 230026, PR China

[§]High Magnetic Field Laboratory, Chinese Academy of Sciences, Hefei, Anhui 230031, PR China

S *Supporting Information*

ABSTRACT: Fabricating a flexible room-temperature ferromagnetic resistive-switching random access memory (RRAM) device is of fundamental importance to integrate nonvolatile memory and spintronics both in theory and practice for modern information technology and has the potential to bring about revolutionary new foldable information-storage devices. Here, we show that a relatively low operating voltage (+1.4 V/ −1.5 V, the corresponding electric field is around 20 000 V/ cm) drives the dual vacancies evolution in ultrathin SnO_2

SnO_2 nanosheets with different defects types → *realizing the reversible transition between semiconductor and half-metal*

nanosheets at room temperature, which causes the reversible transition between semiconductor and half-metal, accompanyied by an abrupt conductivity change up to 10^3 times, exhibiting room-temperature ferromagnetism in two resistance states. Positron annihilation spectroscopy and electron spin resonance results show that the Sn/O dual vacancies in the ultrathin SnO_2 nanosheets evolve to isolated Sn vacancy under electric field, accounting for the switching behavior of SnO_2 ultrathin nanosheets; on the other hand, the different defect types correspond to different conduction natures, realizing the transition between semiconductor and half-metal. Our result represents a crucial step to create new a information-storage device realizing the reversible transition between semiconductor and half-metal with flexibility and room-temperature ferromagnetism at low energy consumption. The as-obtained half-metal in the low-resistance state broadens the application of the device in spintronics and the semiconductor to half-metal transition on the basis of defects evolution and also opens up a new avenue for exploring random access memory mechanisms and finding new half-metals for spintronics.
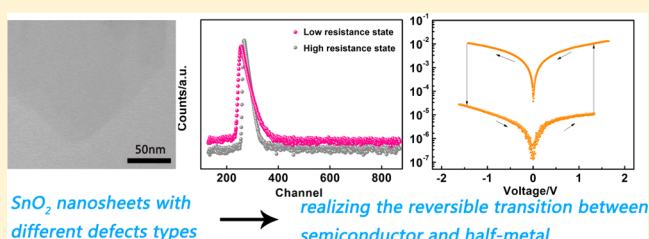
■ INTRODUCTION

Modern information-storage technologies have attracted much research attention, which is converting from traditional Si-based technologies, suffering from performance degradation because of the scaling limit, to nonvolatile memory technologies.[1,2] Resistive-switching random access memory (RRAM), functioning as the most promising competitor of nonvolatile memory thanks to its simple fabrication process, high response speed, high density memory, and low energy consumption,[3,4] is expected to be a next-generation technology in information-storage field. Furthermore, the great advancement of spintronics mainly constructed by magnetic substances,[5,6] which is regarded as a technology with enormous potential to replace the traditional silicon-based one, is getting increasingly more attention nowadays. On the other hand, transparent flexible devices, offering the great superiorities of being bendable, foldable, implantable, and portable,[7,8] have become a central issue in the fabrication of devices. Thus, we are inspired to explore the flexible room-temperature ferromagnetic

RRAM device to enlighten the next-generation information-storage device integrating nonvolatile memory and spintronics.

Although ferromagnetism and RRAM can be obtained in multiferroics, it brings us great obstacle to fabricate films possessing superior flexibility via such materials because of their intrinsic structures. In fact, we are confronted with austere challenges to gain excellent flexibility from conventional materials, including bulk and nanoparticles, because the strain in materials leads to cracking and segregation between materials or between materials and substances after bending many times. Recently, atomically thin 2D inorganic materials have attracted more and more attention owing to their vast application prospects in the fabrication of nanodevice. Fortunately, the atomically thin nanosheets present a novel research platform owing great flexibility.[9−13] Meanwhile, the ultrathin nanosheets exhibit unique electromagnetic characteristics owing to more inevitably exposed interior atoms and corresponding

defects structure in the nanosheets,[14−17] providing in principle an effective method to modulate the magnetism and electrical property.

As one of the most promising candidates used in the applications based on semiconductors, tin dioxide (SnO_2) has been intensively investigated in the fields of optoelectronic,[18] sensor,[19] and room temperature ferromagnetism.[20] Meanwhile, the unique characteristics of 2D materials such as the great amount of defects resulting from the great superficial area offer the potential chance to explore distinguishing electrical performance of SnO_2 ultrathin nanosheets. Although SnO_2 is nonlayered, the ultrathin nanosheets with atomically thickness have been successfully synthesized via solvothermal process,[21] providing the opportunity for us to do further research in the unique properties of SnO_2.

Herein, we highlight a flexible room-temperature ferromagnetic RRAM device based on SnO_2 ultrathin nanosheets without doping ferromagnetic elements. The as-prepared SnO_2 ultrathin nanosheets have an abrupt conductivity change up to 10^3 times under electric field, with a relatively small working voltage (1.5 V). To fully explore the mechanism of the switching behavior of SnO_2 ultrathin nanosheets, positron annihilation spectra (PAS) and electron spin resonance (ESR) spectra, regarded as powerful tools in detecting electronegative and electropositive defects which have a determining impact on the electronic structure, were utilized to demonstrate that the Sn/O dual vacancies in the ultrathin SnO_2 nanosheets evolve to isolated Sn vacancy under electric field; this provides significant information for the further modeling of DFT calculations, which clearly reveal the conduction nature of different structure with different defect types. Our work clearly illustrates a new understanding of the resistance-switching mechanism, obtaining half-metal in the low-resistance state (LRS), enlightening the application of RRAM device in spintronics that plays a significant role in information technology.

■ EXPERIMENTAL SECTION

Synthesis of SnO_2 Nanosheets. Ordinary SnO_2 nanosheets were synthesized through a simple one-pot method.[21] The ethylenediamine solution of $SnCl_2$ was prepared with 90 mg of $SnCl_2$·$2H_2O$ and ethylenediamine (30 mL, anhydrous) in a glass vessel, and then stirred vigorously over 1 h. The ethylenediamine solution was subsequently transferred into a 50 mL Teflon-lined autoclave and kept at 180 °C for 48 h. After cooling down naturally, the final brown-yellow product was collected by centrifugation and washed with DI water and ethanol several times. After dry at 60 °C overnight the brown yellow powder was stored in room temperature.

Fabrication of Flexible RRAM Device. First, we synthesized the homogeneous thin SnO_2 film using the cellulose membrane (pore size: 0.22 μm) with the suction filter machine, and the control of amount and concentration of the SnO_2 nanosheet solution helps us to get the films with different thickness. Second, we pressed the thin film on the ITO/PET sheet with small amount of ethanol. Then, acetone was used to dissolve the cellulose membrane, and the acetone was refreshed every 3 h. Finally, we had the SnO_2 thin film on the ITO/PET sheet with a size of 2 cm × 3 cm, with a uniform thickness of 700 nm throughout. A Au network was used as the top electrode, which was pressed closely on the nanosheets-based film deposited on ITO/PET sheet.

Characterization. The morphology and structure of the products were investigated by TEM (JEOL-2010 TEM at an acceleration voltage of 200 kV), X-ray diffraction (XRD, Philips X'Pert Pro Super diffractometer with Cu Kα radiation (λ = 1.54178 Å)), atomic force microscopy (AFM, DI Innova Multimode SPM platform), and X-ray photoelectron spectroscopy (XPS, XRF-1800, acceleration voltage 60 kV), and high-angle annular dark-field (HAADF, JEOL JEM-ARF200F). The ESR measurement was performed on JES-FA200 with microwave frequency of 8750−9650 MHz (X-band). The temperature dependence of the resistances was measured on a Keithley 4200 station with the computer-controlled four-probe technique. The magnetic measurement was carried out with a superconducting quantum interference device magnetometer (SQUID, quantum design MPMS XL-7).

Positron Annihilation Measurement. Positron annihilation spectrometry is a powerful technique to detect the type and relative concentrations of defects or vacancies in materials at the parts per million level.[22,23] We pressed the samples into a 1 mm thick round disc and placed a 5 mCi source of ^{22}Na between two prepared identical samples. The positron lifetime experiments were carried out with a fast−slow coincidence ORTEC system with a time resolution of about 230 ps full width at half-maximum.

Electrical Switching Measurement. The electrical behaviors of SnO_2 nanosheets were measured in a three-electrode system at an electrochemical station (CHI 660B) with a sweeping voltage applied to the top electrode. The flexibility measurement was taken after 1000 bending tests with a bending radius of 7 mm for the device. The endurance of the materials was recorded by voltage sweeping at a readout voltage of 0.1 V.

DFT Calculations. All calculations were performed using the Vienna Ab Initio Simulation Package[24] within the projector-augmented wave approach,[25] utilizing the screened hybrid functional proposed by Heyd, Scuseria, and Ernzerhof (HSE).[26] The value of exact nonlocal exchange (a) was chosen to be 25%. We applied periodic boundary conditions with a vacuum space of 15 Å to avoid the interactions between two sheets in the nearest two unit cells. The energy cutoff and the convergence criteria for energy and force are set to be 600 eV, 1.0×10^{-4} eV, and 0.01 eV Å^{-1}, respectively. The k-point grid for the 2 × 2 × 2 slab is 3 × 3 × 1.

■ RESULTS AND DISCUSSION

Inspired by the above analysis, we synthesized SnO_2 ultrathin nanosheets as an example for the investigation of the effect on electrical properties through the external electric field modulating defect types. Because characterization of an individual single layer by XRD is difficult, the as-prepared ultrathin nanosheets were recollected into powders for the XRD characterization, and the XRD patterns shown in Figure 1a can be indexed to SnO_2 rutile phase (PDF No. 88-0287, International Centre for Diffraction Data, 2003). The near transparency shown in the TEM image (Figure 1b) distinctly implies the 2D morphology of the sample. The AFM image in the Figure 1c further confirms the ultrathin nanosheets architecture. The general thickness of the nanosheets is in a range of 1.3 nm ∼2.0 nm and the sample consists of only a few primitive cells in the specific dimension. The HAADF image shown in Figure 1d gives the direct evidence for the highly preferred [001] orientation in SnO_2 nanosheets. The two mutually perpendicular facets are indexed to (110) and ($\bar{1}$10) facets, and the facet at the angle of 45° for (110) facet can be indexed to (200) facet, according to the theoretical interval of the corresponding facets, strongly implying a high degree of [001] orientation in the nanosheets.

Taking into account the fact that the more exposed interior atoms inevitably induce the formation of defects on the surfaces of the ultrathin nanosheets, which would have an important effect on their electronic structure, it is prerequisite to clearly define the defect types involved in the ultrathin nanosheets. Therefore, in our present work, PAS[27] and ESR, which are regarded as powerful tools to investigate the cation and oxygen defects in oxides, respectively, were utilized to detect and analyze the defects in SnO_2 nanosheets. Figure 2a and Table 1 show the positron lifetime spectrum results of the pristine
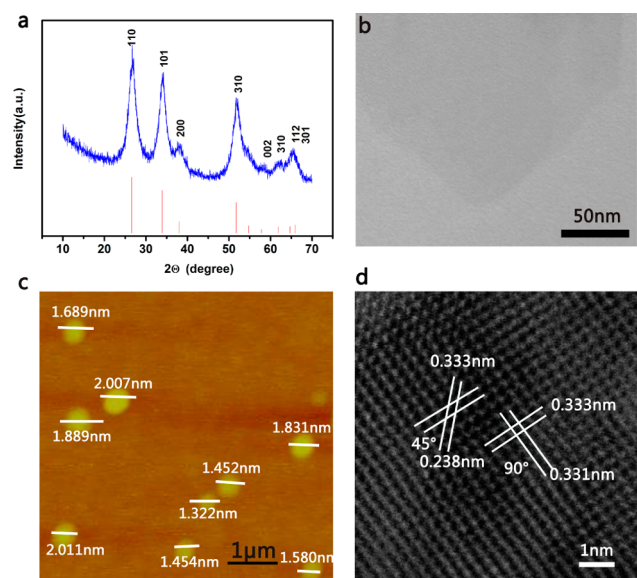
Figure 1. (a) XRD pattern for SnO_2 ultrathin nanosheets. (b) TEM image of SnO_2 ultrathin nanosheets with the feature of transparency and flexibility. (c) Atomic force microscopy (AFM) image of SnO_2 ultrathin nanosheets with an average thickness of 1.30−2.00 nm. (d) High-angle annular dark-field (HAADF) image of SnO_2 ultrathin nanosheets.
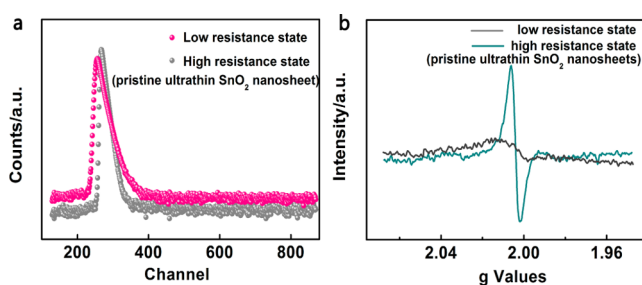

Figure 2. (a) Positron annihilation spectroscopy results of SnO_2 nanosheets in high-resistance state and in low-resistance state. (b) Electron spin resonance results of the SnO_2 nanosheets in high-resistance state and in low-resistance state.

To measure the electric performance of SnO_2 nanosheets that act as active layer, we fabricated the device as shown in Figure 3a. The current versus voltage ($I-V$) curves of the
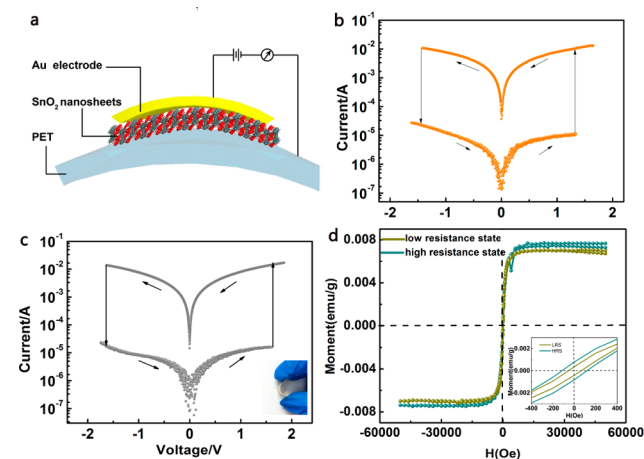

Figure 3. (a) Schematic of Au/SnO_2 ultrathin nanosheets/ITO (PET) device. (b) Current versus voltage curve of the fabricated device (Au/SnO_2 ultrathin nanosheets/ITO (PET) device) with a dc voltage sweeping mode, with a rapid shift from high-resistance state to low-resistance state. (c) Current versus voltage curve obtained from the SnO_2-nanosheets-based device after 1000 bending tests. Inset: photograph of a bent device with a bending radius of 7 mm for the device. (d) $M-H$ curves for the SnO_2 nanosheets in two resistance states measured at 300 K. Inset: the enlarged $M-H$ section in the low applied field.

fabricated devices as measured with a dc voltage sweeping mode is shown in Figure 3b. The voltage is applied to the top Au electrode, and the bottom ITO/PET electrode is grounded during the process. Figure 3b shows the typical $I-V$ curve of Au/SnO_2 ultrathin nanosheets/ITO (PET). When the voltage starts from zero in positive bias, the device first displays a HRS; when the voltage reaches about 1.4 V, the $I-V$ curve suddenly jumps to the LRS. Then, the voltage decreases from positive to zero. During the negative sweep, we decrease the voltage from zero in negative sweep, and the Au/SnO_2 ultrathin nanosheets/ITO (PET) device stays in the LRS until the voltage decreases to about −1.5 V. At this point, the current decreases abruptly, indicating that the device has transformed from the LRS to the HRS. In Figure 2b, the ON/OFF ratio read at 1 V is nearly 1×10^3, which meets the requirement for nonvolatile memory applications. The resistance values of both the HRS and the LRS are stable without degradation over 8×10^4 s and exhibit only small fluctuations in both the states more than 500 cycles as shown in Figure S1. Figure 3c shows that the SnO_2 ultrathin nanosheets-based device has negligible degradation of the set/reset voltage and ON/OFF ratio after 1000 bending cycles and possesses an excellent flexibility. Moreover, the $M-H$ curves presented in Figure 3d provide direct evidence proving the intrinsic room-temperature ferromagnetism of the sample in both the HRS and the LRS, and the ferromagnetism intensities in the two resistance states stay almost unchanged, showing a

ultrathin SnO_2 nanosheets, in which three lifetime components τ_2, τ_3, and τ_4 with relative intensities I_2, I_3 and I_4 were discerned. The longest lifetime component τ_4 in the high-resistance state (HRS) is believed to be the formation and annihilation on the surface of orthopositronium between the radiative source and the sample.[16] The shortest lifetime component τ_2 (229.8 ps) can be attributed to the coexisting Sn and O dual vacancies, and the intermediate lifetime component τ_3 (425.3 ps) is attributed to the large size defects.[27,28] Furthermore, the signal in 2.0040 g value distinctly observed in the pristine ultrathin SnO_2 nanosheet as shown in Figure 2b manifests the existence of isolated oxygen vacancies.[29] According to the emerging dual defects, it is reasonable to expect novel electrical property in the ultrathin nanosheet.

Table 1. Positron Lifetime Results of SnO_2 Nanosheets

sample	τ_1 (ps)	τ_2 (ps)	τ_3 (ps)	τ_4 (ns)	I_1 (%)	I_2 (%)	I_3 (%)	I_4 (%)
high-resistance state (pristine ultrathin SnO_2 nanosheet)		229.8	425.3	1.5		52.8	47.1	0.1
low-resistance state	193.9		413.6	1.1	58.1		41.7	0.2

great potential for the fabrication of flexible room-temperature ferromagnetic resistive-switching nanodevice.

The temperature dependence of resistances diagrams of the two resistance states are shown in Figure S2. The resistance increases when the temperature arises in the LRS, which indicates the semimetallic characteristic in this state. For comparison, Figure S2b shows the decrease of resistance when temperature decreases, which is consistent with the behavior of semiconductor.

To analyze further the effect of the defects in the two resistance states of the nanosheets, we also apply PAS and ESR measurement in the LRSs. As shown in Figure 2b, the concentration of oxygen vacancy in the LRS is much lower than that in the HRS, which indicates the mobility of oxygen vacancies under electric field, resulting in the aggregation of oxygen vacancies, having caused the defects types switching and thus having a great impact on the electric properties. The PAS result in the LRS also gives a direct evidence for the changed defects in the LRS, illustrating that isolated Sn vacancy is the dominant type of defects after the mobility and aggregation of oxygen vacancies under electric field concluded by ESR results. After applying external electric field in the LRS, as seen in Figure 2a and Table 1, the shortest lifetime component τ_1 (193.9 ps) can be attributed to isolated Sn vacancies, and the intermediate lifetime component τ_3 (413.6 ps) is attributed to the large-size defects. The relative intensities of the components in the two resistance states reveal that the dominant electronegative defects (τ_2 component) in SnO_2 nanosheets without applying electric field are the coexisting Sn and O dual vacancies, whereas the dominant electronegative defects (τ_1 component) in SnO_2 nanosheets after applying electric field are isolated Sn vacancies, and both of the states contain large-size defects of which the intensity almost stays the same.

According to the PAS and ESR results, it is reasonable to deduce the mechanism of the switching behavior on the basis of the evolution of defects under electric field. Figure 4 illustrates the mechanism of the switching behavior. When there is no external electric field applied on the film, the forms of defects are coexisting Sn and O vacancies and oxygen vacancy on the basis of the PAS and ESR results. Then, the electric field is applied on the device, the vacancy complexes start to separate, mostly because of the mobility of oxygen vacancies which has been confirmed by ESR results. After the accumulation of oxygen vacancies with the actuation of electric field force to the cathode (Figure 4c), the previous Sn vacancies in the coexisting Sn and O vacancies become isolated Sn vacancy. When the opposite electric field is applied, the oxygen vacancies start to move to another pole of the film, mixing with the isolated Sn vacancies and making coexisting Sn and O vacancies again as shown in Figure 4d.

To figure out the roles that coexisting Sn and O dual vacancies, isolated Sn vacancies, and isolated O vacancies play in the resistive-switching behavior and explore the nature of the metallic characteristic in the two resistance state on the basis of experimental results, DFT calculations were performed to model the concrete structure.

The structure we use is a 2 × 2 × 2 supercell containing 48 atoms exposing (001) facet, of which the thickness is 0.64 nm, very close to that of the realistic system because of the ultrathin thickness of the specimen. Considering the variable distances between the Sn vacancy and the O vacancy, we calculated the total energies of several systems with different feasible positions
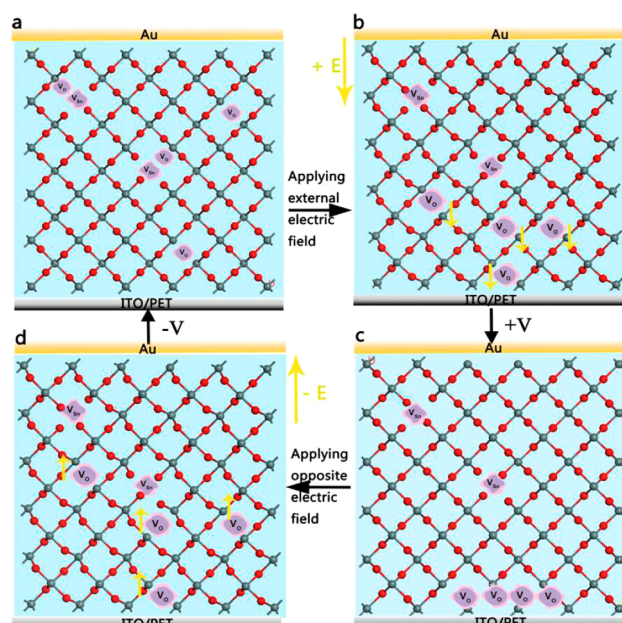

Figure 4. (a) Coexisting Sn and O vacancies and isolated oxygen vacancy are the majority of the defects in SnO_2 nanosheets with no applied electric field. (b) Coexisting Sn and O vacancies start to separate and the oxygen vacancies move toward cathode with the actuation of electric field. (c) Oxygen vacancies accumulate in the cathode. (d) Oxygen vacancies move back and mix up with the isolated Sn vacancies to form the coexisting Sn and O vacancies when applying opposite electric field.

where the coexisting Sn and O vacancies locate to find the most stable one for the subsequent calculation. The result shown in Figure S3a, manifesting the most stable structure containing one Sn vacancy and O vacancy, has the minimum distance, which is 2.052 Å, and the positions of Sn vacancy and O vacancy are shown in Figure S3b. The other models we chose to do the energy calculations for are listed in Supporting Information.

Figure 5a,b displays the calculated density of states (DOSs) of the 2 × 2 × 2 atomically thin SnO_2 slab, with the coexistence of Sn and O vacancies and an isolated Sn vacancy. The slab of the coexisting of Sn and O vacancies shows semiconductive behavior, consistent with the experimental results that SnO_2 nanosheets without applying external electric field are semiconductive. The slab containing one isolated Sn vacancy shows a half-metallic characteristic, mostly originating from the O 2p state, accounting for the metallic nature of SnO_2 nanosheets in the LRS after applying external electric field. The model with one oxygen vacancy is semiconductive as shown in Figure S4, indicating that the O vacancy which is confirmed to exist in the nanosheets in two resistance states by ESR results has no attribution to the half-metallic characteristic caused by the isolated Sn vacancy in the LRS. Because of the mobility of oxygen vacancies, the isolated Sn vacancies appear repeatedly. Consequently, the semiconductive state and half-metallic state will transform mutually on the basis of the defects structures under the modulation of external electric field, providing a new understanding for the mechanism of switching behavior. Most interestingly, it is worth noting that the half-metal has continuously attracted much attention because of its highly spin-polarized carriers, acting as the most ideal candidate for spintronics.[30−32] However, the strong temperature dependence of spin polarization in most of the reported half-metals[33,34]
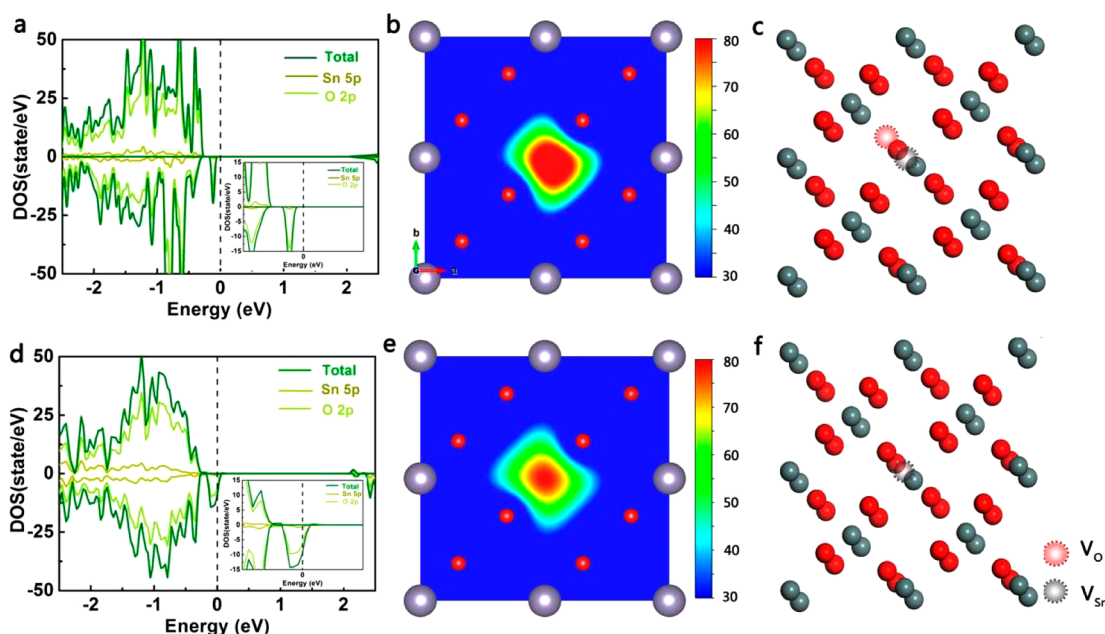
Figure 5. (a) Density of state (DOS) diagram of the structure with coexisting Sn and O vacancies. (b) Schematic representation of trapped positrons of coexisting Sn and O vacancies. (c) Slab ($2 \times 2 \times 2$) with the coexisting Sn and O vacancies. (d) DOS diagram of the structure with isolated Sn vacancy. (e) Schematic representation of trapped positrons of isolated Sn vacancy. (f) Slab ($2 \times 2 \times 2$) with an isolated Sn vacancy.

indicates that the spin polarization is usually obtained at extremely low temperature which limits their practical applications. In the present work, we developed a new method to create half-metal in a temperature independent manner from intrinsic semiconductor on the basis of the modulation of defect by electric field, which undoubtedly opens up a new avenue for exploring highly spin-polarized half-metal.

CONCLUSIONS

We highlight ultrathin SnO_2 nanosheets with atomic thickness as a promising material to construct a flexible room-temperature ferromagnetic resistive-switching device. The positron annihilation spectra and electron spin resonance spectra clearly demonstrated that the Sn/O dual vacancies in the ultrathin SnO_2 nanosheets evolve to isolated Sn vacancy under electric field. Derived from this vacancies evolution and concluded from the DFT calculation results, the ultrathin SnO_2 nanosheets realize reversible transition between semiconductor and half-metal, accounting for the switching behavior and providing a new understanding for the switching mechanism. In addition, this ultrathin nanosheets-based RRAM device also shows excellent flexibility, opening up opportunities for exploring new 2D materials for flexible electronic device. Most importantly, the half-metal obtained through the extra electric field manipulating the defect in ultrathin nanosheets is temperature-independent and easily accessible and has good stability and cyclability, which undoubtedly broadens the strategy to obtain half-metals, greatly inspiring the fabrication of spintronics devices.

ASSOCIATED CONTENT

Ⓢ Supporting Information

The Supporting Information is available free of charge on the ACS Publications website at DOI: 10.1021/jacs.5b10212.

Temperature dependence of resistance diagram of LRS and HRS; stability and cyclability of the Au/SnO_2 ultrathin nanosheets/ITO (PET) device; and DFT calculations for more structures. (PDF)

AUTHOR INFORMATION

Corresponding Authors

*cxiao@ustc.edu.cn
*yxie@ustc.edu.cn

Author Contributions

M.L. and Y.L. contributed equally to this work.

Notes

The authors declare no competing financial interest.

REFERENCES

(1) Borghetti, J.; Snider, G. S.; Kuekes, P. J.; Yang, J. J.; Stewart, D. R.; Williams, R. S. *Nature* **2010**, *464*, 873.

(2) Kwon, D. H.; Kim, K. M.; Jang, J. H.; Jeon, J. M.; Lee, M. H.; Kim, G. H.; Li, X.-S.; Park, G.-S.; Lee, B.; Han, S. *Nat. Nanotechnol.* **2010**, *5*, 148.

(3) Waser, R.; Aono, M. *Nat. Mater.* **2007**, *6*, 833.

(4) Linn, E.; Rosezin, R.; Kugeler, C.; Waser, R. *Nat. Mater.* **2010**, *9*, 403.

(5) Ohno, H. *Nat. Mater.* **2010**, *9*, 952.

(6) Singh, A. K.; Yakobson, B. I. *Nano Lett.* **2009**, *9*, 1540.

(7) Sup Choi, M.; Lee, G.-H.; Yu, Y.-J.; Lee, D. Y.; Hwan Lee, S.; Kim, P.; Hone, J.; Jong Yoo, W. *Nat. Commun.* **2013**, *4*, 1624.

(8) Kim, S.; Jeong, H. Y.; Kim, S. K.; Choi, S.-Y.; Lee, K. J. *Nano Lett.* **2011**, *11*, 5438.

(9) Yang, J. J.; Strukov, D. B.; Stewart, D. R. *Nat. Nanotechnol.* **2012**, *8*, 13.

(10) Zhu, H.; Xiao, C.; Cheng, H.; Grote, F.; Zhang, X.; Yao, T.; Li, Z.; Wang, C.; Wei, S.; Lei, Y.; Xie, Y. *Nat. Commun.* **2014**, *5*, 3960.

(11) Liu, J.; Yin, Z.; Cao, X.; Zhao, F.; Wang, L.; Huang, W.; Zhang, H. *Adv. Mater.* **2013**, *25*, 233.

(12) Liu, J.; Zeng, Z.; Cao, X.; Lu, G.; Wang, L. H.; Fan, Q. L.; Huang, W.; Zhang, H. *Small* **2012**, *8*, 3517.

(13) He, Q.; Zeng, Z.; Yin, Z.; Li, H.; Wu, S.; Huang, X.; Zhang, H. *Small* **2012**, *8*, 2994.

(14) Sun, Y.; Gao, S.; Xie, Y. *Chem. Soc. Rev.* **2014**, *43*, 530.

(15) Wu, C.; Feng, F.; Xie, Y. *Chem. Soc. Rev.* **2013**, *42*, 5157.

(16) Butler, S. Z.; Hollen, S. M.; Cao, L.; Cui, Y.; Gupta, J. A.; Gutiérrez, H. R.; Heinz, T. F.; Hong, S. S.; Huang, J.; Ismach, A. F.; et al. *ACS Nano* **2013**, *7*, 2898.

(17) Sun, Y.; Gao, S.; Lei, F.; Xiao, C.; Xie, Y. *Acc. Chem. Res.* **2015**, *48*, 3.

(18) Kuang, Q.; Jiang, Z.-Y.; Xie, Z.-X.; Lin, S.-C.; Lin, Z.-W.; Xie, S.-Y.; Huang, R.-B.; Zheng, L.-S. *J. Am. Chem. Soc.* **2005**, *127*, 11777.

(19) Kuang, Q.; Lao, C.; Wang, Z. L.; Xie, Z.; Zheng, L. *J. Am. Chem. Soc.* **2007**, *129*, 6070.

(20) Coey, J. M. D.; Venkatesan, M.; Fitzgerald, C. B. *Nat. Mater.* **2005**, *4*, 173.

(21) Sun, Y.; Lei, F.; Gao, S.; Pan, B.; Zhou, J.; Xie, Y. *Angew. Chem.* **2013**, *125*, 10763.

(22) Boroński, E.; Nieminen, R. M. *Phys. Rev. B: Condens. Matter Mater. Phys.* **1986**, *34*, 3820.

(23) Perdew, J. P.; Burke, K.; Ernzerhof, M. *Phys. Rev. Lett.* **1996**, *77*, 3865.

(24) Kresse, G.; Furthmüller. *Phys. Rev. B: Condens. Matter Mater. Phys.* **1996**, *54*, 11169.

(25) Kresse, G.; Joubert, D. *Phys. Rev. B: Condens. Matter Mater. Phys.* **1999**, *59*, 1758.

(26) Heyd, J.; Scuseria, G. E.; Ernzerhof, M. *J. Chem. Phys.* **2003**, *118*, 8207.

(27) Shek, C. H.; Lai, J. K. L.; Lin, G. M. *J. Phys. Chem. Solids* **1999**, *60*, 189.

(28) Liu, X.; Zhou, K.; Wang, L.; Wang, B.; Li, Y. *J. Am. Chem. Soc.* **2009**, *131*, 3140.

(29) Gordon, T. R.; Cargnello, M.; Paik, T.; Mangolini, F.; Weber, R. T.; Fornasiero, P.; Murray, C. B. *J. Am. Chem. Soc.* **2012**, *134*, 6751.

(30) Wolf, S. A.; Awschalom, D. D.; Buhrman, R. A.; Daughton, J. M.; Von Molnar, S.; Roukes, M. L.; Treger, D. M. *Science* **2001**, *294*, 1488.

(31) Žutić, I.; Fabian, J.; Das Sarma, S. *Rev. Mod. Phys.* **2004**, *76*, 323.

(32) Wang, H.; Zhang, J.; Hang, X.; Zhang, X.; Xie, J.; Pan, B.; Xie, Y. *Angew. Chem.* **2015**, *127*, 1211.

(33) Hasegawa, K.; Isobe, M.; Yamauchi, T.; Ueda, H.; Yamaura, J. I.; Gotou, H.; Yagi, T.; Sato, H.; Ueda, Y. *Phys. Rev. Lett.* **2009**, *103*, 146403.

(34) Villamor, E.; Isasa, M.; Hueso, L. E.; Casanova, F. *Phys. Rev. B: Condens. Matter Mater. Phys.* **2013**, *88*, 184411.